



High-Bandwidth Low-Inductance Current Shunt for Wide-Bandgap Devices Dynamic Characterization

Wen Zhang , Student Member, IEEE, Zheyu Zhang , Senior Member, IEEE, Fred Wang, Fellow, IEEE, Edward V. Brush, and Neil Forcier

Abstract—High bandwidth sensors are required to measure the wide-bandgap devices' transient behavior because of their fast switching speed. In addition to high bandwidth, the current sensor must introduce little extra parasitic inductance to the switching power loop. The analysis of conventional shunt resistors shows the key to high bandwidth is the coaxial structure and its parasitic inductance is proportional to its transient heat energy rating. By combining the structure of coaxial shunt resistor and alumina substrate surface mount thin film resistors, a novel surface mount coaxial shunt resistor is introduced. Experimental measurement verifies its capability of achieving very high bandwidth while introducing very low parasitic inductance. The design can achieve up to 2.23-GHz measurement bandwidth while keeping its parasitic inductance as low as 0.12 nH. Application in gallium nitride heterojunction-field-effect-transistors double pulse test shows it can faithfully capture the transient current waveform while introducing little interference to the switching behavior.

Index Terms—Current sensor, double pulse test (DPT), measurement bandwidth, network analyzer, parasitic inductance, wide-bandgap devices.

I. INTRODUCTION

SEMICONDUCTOR switches are the foundation of power electronics converters. Wide-bandgap materials, especially silicon carbide (SiC) and gallium nitride (GaN), exhibit superior physical properties compared to silicon, making them very appealing for power electronics applications [1]. Promising as they are, their wider adoption requires crucial semiconductor device information, including both the static and dynamic

Manuscript received May 19, 2020; revised August 5, 2020; accepted September 10, 2020. Date of publication September 23, 2020; date of current version November 20, 2020. This work was supported in part by Keysight Technologies through CURENT industry membership. This work made use of Engineering Research Center shared facilities supported in part by the Engineering Research Program of the National Science Foundation, in part by the Department of Energy under NSF Award EEC-1041877, and in part by the CURENT Industry Partnership Program. Recommended for publication by Associate Editor Dr. C. N. M. Ho (Corresponding author: Wen Zhang.)

Wen Zhang is with the EECS, University of Tennessee, Knoxville, TN 37996 USA (e-mail: wzhang53@vols.utk.edu).

Zheyu Zhang is with the Electrical and Computer Engineering, Clemson University, North Charleston, SC 29405 USA (e-mail: zheyu.zhang@ieee.org).

Fred Wang is with the Department of Electrical Engineering and Computer Science, University of Tennessee, Knoxville, TN 37996 USA (e-mail: fred.wang@utk.edu).

Edward V. Brush and Neil Forcier are with the Keysight Technologies, Santa Rosa, CA 95403 USA (e-mail: brush@keysight.com; neil_forcier@keysight.com).

Color versions of one or more of the figures in this article are available online at <https://ieeexplore.ieee.org>.

Digital Object Identifier 10.1109/TPEL.2020.3026262

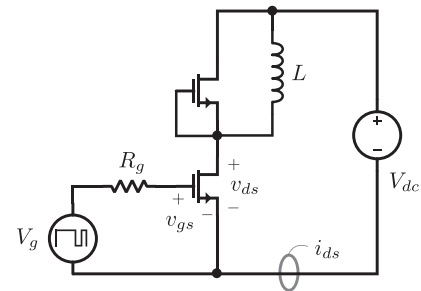


Fig. 1. Double pulse test setup simplified circuit schematic.

characteristics. While the static characteristics can be relatively easily obtained on a curve tracer, the dynamic characteristics including the switching transient energy loss and switching time require dedicated experimental setup like the double pulse test (DPT) [2]. The captured switching transient waveforms are also crucial for modeling and understanding their transient behavior.

The general DPT setup circuit schematic is shown in Fig. 1. Three measurements are usually required, including the gate-source voltage v_{gs} , drain-source voltage v_{ds} , and drain current i_{ds} . The impact of voltage measurements to the switching transient is usually negligible because of their very large input impedances, typically in the range of $M\Omega$. However, the current measurement is much more challenging because of its intrusive nature. The current signal must be converted to voltage before being measured and recorded with oscilloscopes. Furthermore, the current sensor must have sufficient measurement bandwidth to capture the switching transient with high fidelity. Take the 650 V-GaN heterojunction-field-effect-transistors (HFETs) DPT as an example, the power loop inductance is typically very small and can be less than 3.0 nH due to their more compact package [3], [4]. An ideal current sensor would introduce a parasitic inductance much lower than this. The device parasitic capacitances are also much smaller because of the smaller die size. As a result, the oscillation frequency determined by the parasitic inductance and capacitance is quite high and can be up to 300 MHz. Since the measurement bandwidth is often defined by the 3-dB point in its transfer function, the current sensor should have higher bandwidth than the power loop oscillation frequency to avoid any signal distortion.

Several types of current sensors have been applied in DPT, including resistive current sensor, Rogowski coil and current transformer. Resistive current sensors or shunts use the Ohm's law for a direct current-to-voltage conversion, typically with

high precision and low temperature drift resistors. State-of-the-art coaxial shunt resistors use the coaxial structure to effectively cancel the flux coupling between the power loop and the measurement loop and claim up to 2.0-GHz measurement bandwidth [5]. However, the parasitic inductance is around 2.2 nH and the inconsistent measurement bandwidth may adversely affect the accuracy and validity of the measurement [6]. To tackle the large parasitic inductance problem, attempts have been made to use the small package surface mount resistors, specifically thin film resistors, where thin film resistive material is deposited on a ceramic substrate [7]. The ceramic substrate can effectively absorb and dissipate the heat generated by the resistive material. However, surface mount components are usually soldered on a flat printed circuit board (PCB) and therefore it is usually difficult to achieve flux cancellation like the coaxial shunt resistor. An effective approach to achieve higher bandwidth is having several resistors in parallel and connecting the sensing wire in the center region where the flux density is the weakest [3], [8], [9]. However, the reported simulated measurement bandwidth is lower than 200 MHz in [3] when the resistance is 0.1 Ω and 38% error in the transient current measurement is reported. This approach is further improved by separating the paralleled resistors into two groups and leaving a gap in the middle, creating an even weaker magnetic field region [10]. This approach achieves more than 500 MHz bandwidth in simulation but at the sake of increasing the resistance to 1.0 Ω . The authors in [11] experimented with placing the surface mount resistors either in a radial or coaxial configuration but did not report measurement bandwidth. The components used are relatively bulky which results in a large distortion in the measured current waveform. More importantly, these works did not discuss the transient thermal impact or provide the measurement bandwidth directly.

Rogowski coils are another type of current sensors where the current signal is reconstructed by integrating the current derivative signal from a helix coil wound around an amagnetic skeleton. A major benefit of Rogowski coil is the electrical isolation between the primary side circuit and the measurement. However, the state-of-the-art commercial Rogowski coil with a sensitivity of 100 mV/A only has a higher bandwidth of 50 MHz, which is far from sufficient [12]. By performing the integration digitally and sacrificing the lower bandwidth, it has been reported that the bandwidth can be increased to about 225 MHz [13]. Current transformers, another type of current sensors based on Faraday's law of induction, may offer up to 250-MHz bandwidth according to some commercial products, although the cross-sectional area is around 60.0 mm² [14]. Unlike Rogowski coils, current transformers use magnetic cores and suffer from saturation. As a result, the cross-sectional area or the extra power loop area introduced to the DPT power stage can be very large.

In summary, there is a technical gap between the state-of-the-art current sensor and the measurement requirements from DPT, especially for high speed GaN HFETs. The resistive sensor approach is further analyzed to understand its theoretical limitation. It is found the shunt's energy rating is proportional to its parasitic inductance, and DPT's typical energy dissipation means the size of the current shunt can be drastically

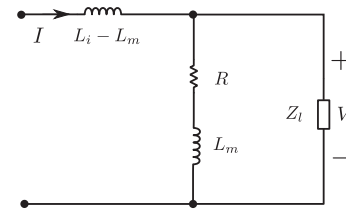


Fig. 2. Resistive current sensor equivalent circuit.

shrunk. A novel implementation of current shunt mimicking the coaxial structure with surface mount thin film resistors is then introduced. Detailed electrical and thermal modeling of several design variants are carried out. In simulation, up to GHz measurement bandwidth can be achieved with the proposed implementation while keeping the parasitic inductance below 0.27 nH. In the worst case, the transient temperature rise results in less than 1.0% measurement uncertainty due to resistance drift. The electrical models are verified in experiments and in the best case, the parasitic inductance is found to be 0.12 nH while the measurement bandwidth is 2.23 GHz. The measurement validity is further verified in GaN HFETs DPT experiments. The switching transient current waveform is captured faithfully and very little interference to the switching behavior is observed.

II. RESISTIVE CURRENT SENSORS

Current sensing invariably involves converting the current signal to voltage signal for the oscilloscope or other test equipment. The easiest and most direct way to do so is making the current flow through a resistor. Ideally the voltage across the resistor will be proportional to the current based on Ohm's law $V = R \cdot I$. The equivalent circuit for a general resistive sensing approach is shown in Fig. 2. However, in practice, resistors must take finite physical space and the current flow through it will generate magnetic field around it, introducing an equivalent parasitic inductor. This inductor, inserted inside the switching power loop, is denoted as L_i . The voltage across the resistor is passed to either the oscilloscope or other signal processing circuitry through a pair of conductors or a transmission line, and therefore making the sensing resistor a two-terminal device. The impedance of sensing wires connected with the test equipment is denoted as Z_l . Since the equipment impedance Z_l is essentially in parallel with resistor, it must exhibit much higher impedance than the resistor to avoid any interference and drawing too much power from the measured circuit. Typically, the measurement instrument is an oscilloscope with a termination impedance of $Z_l = 50 \Omega$. A transmission line with a matching characteristic impedance of 50 Ω is used for the connection to avoid any wave reflection.

Considering the magnetic field distribution around the resistor, if sensing wires enclose part of it, the voltage picked up and sent to the test equipment includes part of inductive voltage drop as well. The equivalent inductance is the mutual inductance between the switching power loop and the measurement loop. It is therefore denoted as L_m . Note that the capacitive parasitic elements are not included in the model here because the sensors

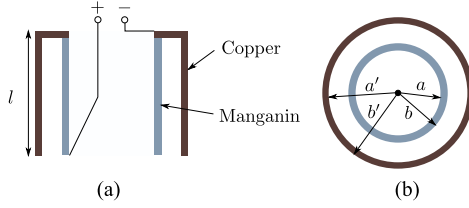


Fig. 3. Physical structure of a coaxial shunt resistor. (a) Side cross-section. (b) Top cross-section.

are typically designed so that they negligible, such as the coaxial shunt resistor [9].

Assuming $|R + j\omega L_m| \ll |Z_l|$, it is obvious that the transfer function of the measured current to the voltage across the oscilloscope is

$$G_{vi}(j\omega) = \frac{V}{I} = R + j\omega L_m. \quad (1)$$

The parasitic inductance that is only in the power loop $L_i - L_m$ is in series with the measured current I and therefore does not show up in the transfer function. But it might alter the semiconductor device switching transient behavior and therefore must be kept low. Note that, in the frequency domain, the magnitude of G_{vi} is increasing at +20 dB/decade beyond its corner frequency because of the mutual inductance L_m . The corner frequency (3-dB point) or the bandwidth for a general resistive current sensor whose $L_m \neq 0$ is given by

$$f_r = \frac{R}{2\pi L_m}. \quad (2)$$

A. Coaxial Shunt Resistor

The coaxial shunt resistor is a relatively old concept [9], where the flux coupling between the power loop and the measurement loop are negated in a coaxial structure. The typical coaxial shunt resistor uses material with good conductivity such as copper for the outer shell. The inner shell is made of another material with higher resistivity and low thermal drift, which can be Manganin [15]. The physical structure of a coaxial shunt resistor is shown in Fig. 3.

The dc resistance of the coaxial shunt resistor is given by

$$R_{dc} = \frac{\rho l}{\pi(b^2 - a^2)} \approx \frac{\rho l}{2\pi a(b - a)} \quad (3)$$

where l is the length of the coaxial shunt resistor, a and b are the inner and outer diameter of the resistor, respectively, and ρ is the resistivity of the inner shell material.

Ideally, the magnetic field of the coaxial shunt resistor only exists between the inner and outer shell. By placing the pickup wires inside the inner shell, there is no flux coupling and $L_m \rightarrow 0$. Therefore the measurement bandwidth can be very high. Ultimately, the bandwidth is limited by the skin effect as the current crowds at the conductor's surface which increases the effective resistance at higher frequency. The ac resistance of a coaxial shunt resistor is given by

$$R_{ac} = \frac{l}{\pi b} \sqrt{\frac{\omega \mu_0 \mu_r \rho}{2}}. \quad (4)$$

The bandwidth of a coaxial shunt resistor can be found by equating Figs. 3 and 4

$$f_{bw} = \frac{\rho}{\pi \mu_0 \mu_r (b - a)^2}. \quad (5)$$

B. Energy Rating and Physical Footprint

In addition to the bandwidth, the parasitic inductance L_i is another important parameter for DPT as it may severely alter the switching behavior. The parasitic inductance of a coaxial shunt resistor when the inner shell is thin enough can be written as

$$L_i = \frac{\mu_0 l}{2\pi} \ln\left(\frac{a'}{b}\right). \quad (6)$$

It appears the inductance can be made infinitely small if the gap between the inner and outer shell is infinitely small. As the gap between the outer copper shell and inner Manganin shell shrinks, the parasitic capacitance increases. Assuming the gap is filled with air, the parasitic capacitance is given by

$$C_p = \frac{2\pi \epsilon_0 l}{\ln\left(\frac{a'}{b}\right)}. \quad (7)$$

If the gap ($a' - b$) is too small, the parasitic capacitance C_p in parallel with the resistance and the gain G_{vi} becomes capacitance at higher frequencies, which should be avoided for coaxial shunt resistors [9]. The corner frequency determined by $(2\pi RC_p)^{-1}$ must be much higher than the bandwidth determined by skin effect f_{bw}

$$\frac{1}{2\pi RC_p} = k \cdot f_{bw} \quad (8)$$

where $k \gg 10$. Looking at Fig. 6, another opportunity of shrinking the parasitic inductance L_i is having a shorter length l . Given a fixed bandwidth which means fixed inner shell thickness, Fig. 3 tells us the radius of the inner shell a should decrease proportionally with l to keep the resistance the same. Both thickness $(b - a)$ and length l decreasing together means the mass of the resistive shell is decreasing as well

$$m \approx 2\pi \rho_m l a (b - a) \quad (9)$$

where ρ_m is the resistive material density. In a pulse current measurement application as DPT, the current passing through the resistor invariably generates Joule heat. Assuming all the energy is dissipated evenly inside the resistive material, the transient temperature rise is another physical limitation of coaxial shunt resistor.

$$\Delta T = \frac{E}{cm} \quad (10)$$

where E is the thermal energy dissipated and c is the thermal mass capacity. The transient temperature rise ΔT must be kept in a reasonable range to avoid measurement inaccuracy or material destruction. For example, although Manganin has a very low resistivity thermal drift of $1.8 \times 10^{-6}/K$, it has a maximum application temperature in air of $140^\circ C$ [15] and therefore it is typically required that $\Delta T \leq 100^\circ C$ at room temperature [9].

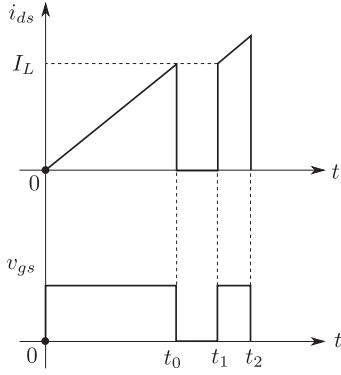


Fig. 4. Double pulse test example current waveform.

From the analysis above, it is evident that the resistance R , bandwidth f_{bw} , and transient energy rating E completely define a coaxial shunt resistor design. Solving the design and plugging it back into Fig. 6, we have

$$L_i = \frac{2\pi k \mu_0 \epsilon_0 R^2 f_{bw} E}{c \rho_m \rho \Delta T}. \quad (11)$$

Therefore, given a resistive material such as Manganin and desired resistance R and bandwidth f_{bw} , the parasitic inductance L_i is solely dependent on and linearly proportional to the energy rating E . Note that all previous analysis on coaxial shunt resistor is based on an ideal implementation. However, nonideality has been observed with commercial products where the measurement bandwidth varies significantly between different samples [6].

C. Practical Energy Requirement

In DPT, the current in the current sensor should always rise linearly as the voltage is immediately applied across the load inductor when the lower switch is ON. The typical current waveform is shown in Fig. 4. Considering the normal condition, suppose the total current conduction time in the first and second pulse is $t_d = t_0 + (t_2 - t_1)$, the energy dissipated in the coaxial shunt resistor is given by

$$E = \int_0^{t_d} i_{ds}^2 R dt = \int_0^{t_d} \left(\frac{V_{dc} t}{L} \right)^2 R dt \approx \frac{R L I_L^3}{3 V_{dc}}. \quad (12)$$

The energy rating greatly depends with setup and testing conditions. However, Fig. 12 can be further simplified by applying a general rule of thumb for load inductance in double pulse test [16]

$$L \geq \frac{V_{dc}}{k_i I_L} t_{sw} \quad (13)$$

where k_i is the percentage of the load current ripple during the switching transient and t_{sw} is the total switching event duration.

The resistance R is often selected so that it maximizes the voltage sent to the oscilloscope without exceeding its tolerance, and introduces little damping to the switching transient. Given oscilloscopes' typical maximum dynamic range is 10 V when terminated at 50 Ω , and considering there should be some margin

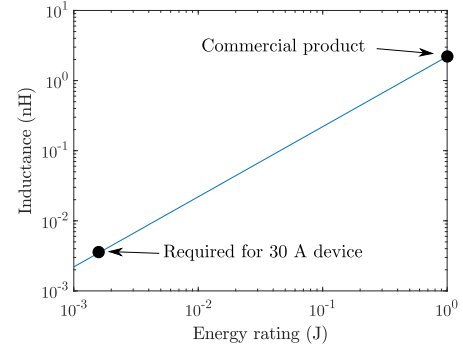


Fig. 5. Relationship between coaxial shunt resistor energy rating and its parasitic inductance.

left for the switching transient oscillation, we can estimate that

$$R I_L \approx 5.0 \text{ V}. \quad (14)$$

Plugging these assumptions back to Fig. 12, we have

$$E \geq \frac{(5.0 \text{ V}) I_L t_{sw}}{3 k_i}. \quad (15)$$

Therefore, the energy rating E for resistive sensors increases proportionally with the load current I_L and the switching transient duration t_{sw} . As an example, the commercial coaxial shunt resistor whose resistance is 0.1 Ω , bandwidth is 2.0 GHz, and energy rating is 1.0 J has an inductance of around 2.2 nH [6], [17]. Assuming conservatively for GaN HFETs that $t_{sw} \approx 300$ ns and $k_i \approx 0.01$, the energy rating required for a 30-A device is only 1.5 mJ. This is in great contrast to the 1.0-J energy rating of commercial products. The relationship between coaxial shunt resistor energy rating and parasitic inductance is shown in Fig. 5. Considering some margin for the energy rating and assuming the energy rating is reduced to 20 mJ, we can estimate from Fig. 6 that the parasitic inductance can be reduced to 44 pH. It may appear that it is promising to achieve high bandwidth and low inductance current measurement by simply scaling down the design. However, the coaxial shunt resistor in this case will have a length $l = 3.7$ mm and an inner radius $a = 0.338$ mm. Achieving coaxial structure in such a minuscule scale may be challenging and fabrication is likely difficult.

III. SURFACE MOUNT COAXIAL SHUNT RESISTOR

A. Motivation and Concept

In the previous analysis of conventional coaxial shunt resistor, it is clearly shown that the energy rating, or equivalently the transient temperature rise, is one of the determining factors of its physical and electrical footprint. The actual required energy rating for DPT can be much lower which means it is possible to greatly lower the parasitic inductance. However, the major challenge is how to implement the coaxial structure in a minuscule scale. Thin film surface mount resistors could achieve small size and lower parasitic inductance. But it is difficult to recreate the coaxial structure when the footprint is small given thin film resistors are usually soldered on a flat surface.

The surface mount coaxial shunt resistor (SMDCSR) is a way to achieve both small scale and coaxial structure with an

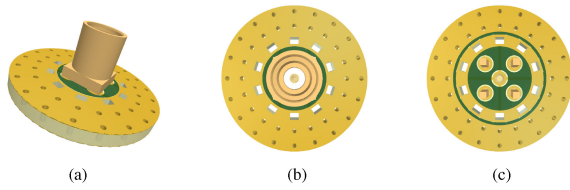


Fig. 6. Surface mount coaxial shunt resistor PCB design #1. (a) Orthogonal view. (b) Top view. (c) Bottom view.

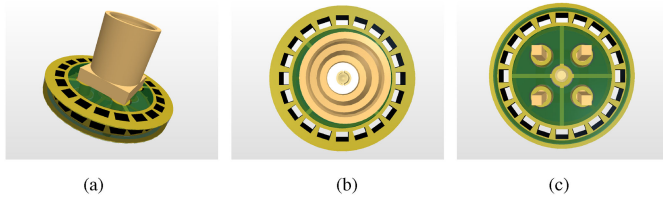


Fig. 7. Surface mount coaxial shunt resistor PCB design #2. (a) Orthogonal view. (b) Top view. (c) Bottom view.

unconventional use of PCB. The PCB design in 3-D is shown in Fig. 6. Small surface mount resistors are inserted into the nonplated rectangular slots. The power loop current flows from the inner copper ring from the bottom side, through the resistors, to the top side copper and then back to bottom outer copper ring through vias or edge plating. A miniature MMCX connector is placed at the center to feed the voltage to an oscilloscope. In the design shown in Fig. 6, there are 10 0402 thin film resistors and the overall diameter of the PCB is 12.7 mm.

The design variables for the SMDCSR include the number of resistors N , resistance value of each resistor R_i , inner radius a , outer radius b , and the length of each resistor l . Because each terminal of resistors must be connected to either the top or bottom side of the PCB, the thickness of the PCB must be the same as or very close to the resistor length l .

From the previous analysis of the traditional coaxial shunt resistors, it is desirable to minimize the gap between the inner and outer shell ($b - a$) as well as the length l for lower parasitic inductance. The thin film resistors should be placed together as tightly as possible to achieve flux cancellation. As a result, the nature of PCB and thin film resistors results in relatively restricted design freedom. The more complex electrical and thermal physical model of SMDCSR also means difficulty in expressing the bandwidth, parasitic inductance, and energy rating in closed-form equations. Therefore, a few different SMDCSR configurations are modeled and characterized to understand the design's capability.

Note that, in the PCB design #1 shown in Fig. 6, the vias are not necessary as edge plated copper can be enough for conducting the return current from the top side to the bottom side. Removing the vias and further increasing the number of resistors in parallel result in the PCB design #2, which is shown in Fig. 7. The diameter is reduced to 8.9 mm.

A total of four SMDCSR example configurations will be discussed here and are listed in Table I. The first two configurations use the PCB design #1. The difference between them is that A has a total resistance of 100 m Ω and B has a total resistance of 10 m Ω . Configurations C and D use the PCB design #2 but C

TABLE I
SMDCSR EXAMPLE CONFIGURATIONS

Config.	A	B	C	D
PCB Design #	1	1	2	2
R (m Ω)	100	10	110	50
No. of resistors N	10	10	20	20

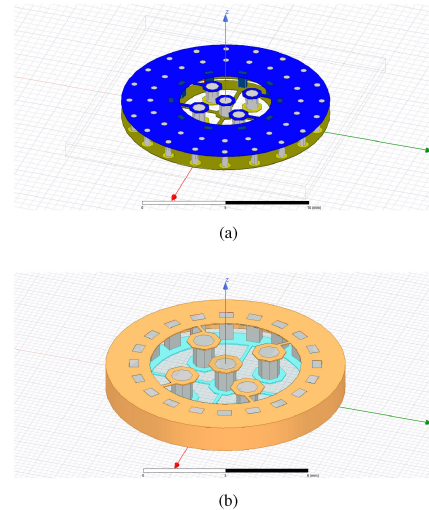


Fig. 8. SMDCSR Q3D models. (a) PCB design #1. (b) PCB design #2.

also D have a resistance of 110 and 50 m Ω , respectively. The reason for #3's seemingly odd resistance is there is 2.2 Ω but no 2.0 Ω in the standard resistance values. From the comparison between the same PCB design, we can evaluate the PCB design's parasitic inductance and understand the energy rating's thermal impact. And by comparing A and C, which have similar total resistance but different PCB design, we can study the impact of tighter resistor placement and better flux decoupling.

B. Electrical Model

Because of the small physical size of SMDCSR, wave propagation can be disregarded, and lumped element circuit is used to describe its electrical behavior. Q3D Extractor is used to obtain the lumped circuit parameters from the physical structure. The models are shown in Fig. 8. Thin film resistors are typically made by depositing a resistive material film on a ceramic substrate which is usually alumina and the resistance is controlled by laser etching [7]. Here, each resistor is modeled as a thin Nichrome layer on top of an alumina substrate because the resistors used in the experiments are made with Nichrome and alumina. Note that due to the lack of resistors' exact geometry information, including the base contact length and laser etching pattern, the model does not necessarily mirror the actual physical implementation.

To directly obtain and visualize the transfer function of SMDCSR, the equivalent circuit for each configuration is exported from the simulation at 1.0 GHz. The resulting SPICE file is simulated in SPICE with frequency sweep. Take C as an example whose simulation result is shown in Fig. 9, when the input current is 1.0 A, the +3-dB point in the output voltage is at around 1.8 GHz. This means C has a bandwidth of around 1.8 GHz. The transfer function gain increases at rate of 20 dB/dec beyond its

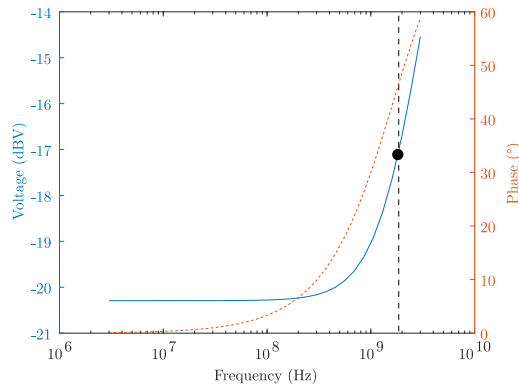


Fig. 9. Bandwidth simulation result of configuration C.

 TABLE II
 Q3D EXTRACTOR SIMULATED SMDCSR BANDWIDTH AND INDUCTANCE

Config. #	A	B	C	D
Bandwidth (MHz)	700	80	1800	1100
Inductance L_i (nH)	0.27	0.27	0.15	0.15

corner frequency, verifying the general resistive current sensor measurement model in Fig. 1. The simulated bandwidths of other configurations are listed in Table II. Comparing A and C, the resistance is similar but the bandwidth is more than doubled. It is clearly shown that having resistors closer together or achieving better flux cancellation increases the bandwidth. Comparing A and B, the same PCB design should have similar mutual inductance L_m and therefore B with 1/10 the resistance value has a bandwidth of about 1/10 of A.

Similarly, the parasitic inductance L_i is also obtained in Q3D as shown in Table II. Note here that the parasitic inductance is only the inductance from the SMDCSR itself and does not include any potential extra power loop area. The inductance is independent of the resistance value and only dependent on the PCB design. Comparing A and C, having more resistors in parallel reduces the parasitic inductance by about 50%. The parasitic inductance values are all very small, less than 0.3 nH.

C. Thermal Model

Compared to Manganin, Nichrome has a much higher working temperature of up to 1400°C, but also a higher thermal drift of $200 \times 10^{-6}/K$. From previous discussion, the transient temperature rise translates into resistance change and therefore measurement uncertainty. The transient temperature rise is simulated in COMSOL and the models are shown in Fig. 10. Similar to the electrical model, each resistor is modeled as a thin Nichrome layer on an alumina substrate. However, only the PCB FR4 substrate is modeled and no copper layers or vias are included. Theoretically, the copper layers and solder joints should help dissipate the heat. Therefore, the model here is conservative and should result in a higher temperature rise than reality.

The transient temperature rise greatly depends on the heat source profile. Consider the same amount of thermal energy, having it all dissipated in a very short period of time means

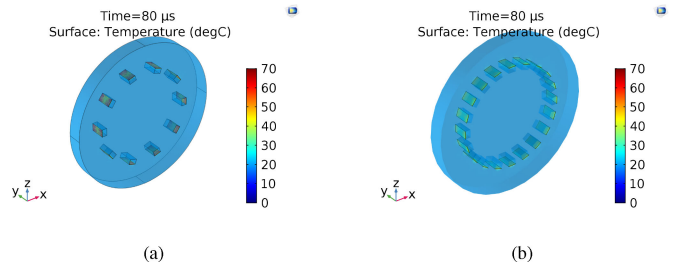


Fig. 10. COMSOL SMDCSR transient thermal simulation model. (a) PCB design #1. (b) PCB design #2.

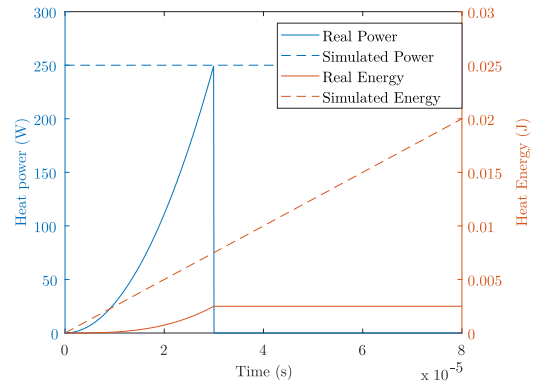


Fig. 11. COMSOL simulation heat source profile compared to reality in DPT.

 TABLE III
 COMSOL SIMULATED SMDCSR TRANSIENT TEMPERATURE RISE

Config. #	A	B	C	D
Max temperature rise °C	45.0	43.6	18.3	18.1
Measurement uncertainty	0.90%	0.87%	0.37%	0.36%

the transient temperature rise is likely concentrated within the resistive material. On the other hand, if the energy is slowly dissipated over a long duration, it is likely that the temperature distributes more evenly across the entire SMDCSR. Therefore, it is critical to have a reasonable but conservative heat source profile to simulate the transient temperature rise.

From previous discussion on energy rating, the transient energy for 50 A is only 2.5 mJ and the total current conduction time is around 30 μs . The current in the load inductor ramps up linearly with time, which means the heat source power $I^2 R$ ramps up quadratically with time. The peak heat power is 250 W. Conservatively, the heat source in the simulation is a constant 250-W source and it is applied for 80 μs . The comparison between the heat source profile in reality and in simulation is shown in Fig. 11. The total dissipated energy is 20 mJ, which is much higher than the energy rating required. At $t = 1 \mu s$, the dissipated energy is already 2.5 mJ. Therefore, the transient temperature rise simulated from COMSOL should be much larger than reality and the results are conservative.

The maximum temperature rise for different SMDCSR configurations are shown in Table III. Note that the temperature rise is also independent of the resistance. This is because the resistive films are very thin and the heat is mostly dissipated to the alumina substrate. Comparing A and C, more than twice as much decrease in maximum temperature rise is observed. This is

the result of having a larger overall contact area with the alumina substrate and therefore more heat is dissipated to the substrate.

Given the commercial thin film resistor with Nichrome material has a thermal drift coefficient of $200 \times 10^{-6}/\text{K}$ [18], the measurement uncertainty due to transient temperature rise can be calculated and is also listed in Table III. In all four configurations, the measurement uncertainty is less than 1.0%, with #3 and #4 achieving less than 0.4%. Considering this is achieved with a drastically more demanding heat source profile, it is shown that SMDCSR has low measurement uncertainty.

IV. EXPERIMENTAL VERIFICATION

A. Measurement Bandwidth

A common way to characterize the measurement bandwidth of coaxial shunt resistors or other resistive current measurement sensor is to apply a well-defined current source, usually of a step function nature, through it and compare the measured voltage against the known current source waveform. An example is to connect it in series with a resistive load in a half-bridge converter [11]. The switch node voltage can be easily measured, from which the current flowing through the coaxial shunt resistor and the load resistor can be derived. However, the bandwidth of coaxial shunt resistors can be up to 2.0 GHz which requires a very sharp rise/fall edge. The frequency content of a rising edge is given by [19]

$$f_c = \frac{0.35}{t_r}. \quad (16)$$

To generate 2-GHz frequency content in a voltage pulse, the rising edge must be no more than 0.18 ns. Although wide-bandgap devices are faster than silicon devices, the power devices today are not nearly fast enough to create a 0.18-ns edge in a resistive-load half bridge.

On the other hand, commercial network analyzers can easily characterize components beyond 100 GHz and retain accuracy for attenuation levels down to -100 dB [20]. The network analyzer directly measures the s -parameters of an electrical network by differentiating the incident wave and reflected wave with directional coupler.

Given the resistive sensor equivalent circuit in Fig. 2, its $ABCD$ matrix can be readily expressed as

$$\begin{aligned} A &= 1 + \frac{j\omega(L_i - L_m)}{R + j\omega L_m} \\ B &= j\omega L_i \\ C &= -1 \\ D &= \frac{1}{R + j\omega L_m}. \end{aligned} \quad (17)$$

The s -parameter S_{21} can be readily obtained from the $ABCD$ matrix

$$S_{21} = \frac{2}{A + B/Z_0 + CZ_0 + D} \quad (18)$$

where Z_0 is the system characteristic impedance and typically $Z_0 = 50 \Omega$.

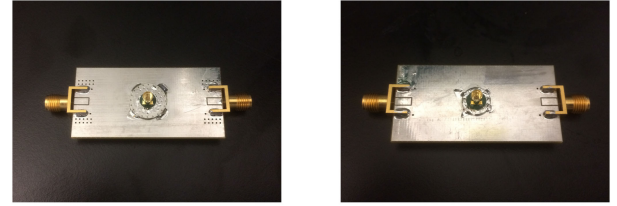


Fig. 12. SMDCSR bandwidth measurement fixtures. (a) SMDCSR PCB design #1 with ten resistors. (b) SMDCSR PCB design #2 with 20 resistors.

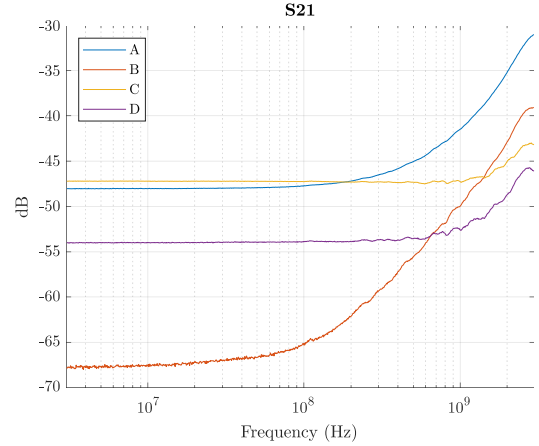


Fig. 13. SMDCSR bandwidth measurement with network analyzer.

Therefore, the transfer response S_{21} of a resistive measurement is given by

$$S_{21} = \frac{2Z_m}{j\omega(L_i - L_m) \left(1 + \frac{Z_m}{Z_0}\right) + 2Z_m + Z_0} \quad (19)$$

where $Z_m = R + j\omega L_m$.

Assuming $|j\omega(L_i - L_m)| \ll Z_0$ and $|Z_m| \ll Z_0$, it can be further simplified as

$$S_{21} = \frac{2(R + j\omega L_m)}{Z_0} = \frac{2G_{vi}}{Z_0}. \quad (20)$$

This means that the transfer response S_{21} from the network analyzer has a linear relationship with the transfer function G_{vi} . For example, ideally a $0.1\text{-}\Omega$ coaxial shunt resistor will have a flat -47.96-dB transfer response. For a general resistive current sensor whose mutual inductance L_m is significant, the transfer response will increase at $+20\text{-dB/dec}$ beyond its corner frequency.

Because the measurement requires a continuous $50\text{-}\Omega$ transmission line to avoid any wave reflection, dedicated microstrip line fixtures are required. The measurement fixtures are shown in Fig. 12. The bandwidth measurement results for the four SMDCSR examples are shown in Fig. 13. The measurement results confirm the resistive current sensor model in Fig. 1. The transfer response increases at a rate of $+20\text{-dB/dec}$ at higher frequency. The bandwidth of each SMDCSR configuration can be obtained by reading the $+3\text{-dB}$ point from their low frequency gain. The bandwidth measurement results are listed in Table IV.

TABLE IV
SMDCSR CONFIGURATIONS BANDWIDTH MEASUREMENT RESULTS

Config. #	A	B	C	D
Bandwidth (MHz)	528	125	2230	1630

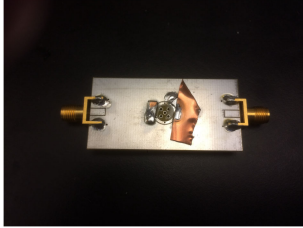


Fig. 14. Impedance analyzer short compensation with SMDCSR fixture.

Generally, the measured results match the model in Q3D Extractor. The difference is probably because of the variations in the manual assembly process. Because of design tolerances, each rectangular slot in the PCB is in fact slightly larger than the thin film resistors. During the assembly process, the thin film resistors could rotate a bit. This results in possibilities that the gaps between resistors are not even. Furthermore, the model assumes a relatively ideal structure for the thin film resistors. In reality, the base contact and laser trimming pattern bring further complication.

In general, A, C, and D can be used for measuring GaN HFETs whose oscillation frequency is up to 300 MHz. As for B, the bandwidth is lower mainly due to its lower resistance. With a resistance of 10 m Ω , B is better suited for measuring higher current rating devices which likely require lower measurement bandwidth.

Interestingly, although the resistance of B is 1/10 of A, the bandwidth of B is 1/5 and not 1/10 of A. Upon closer examination, it is found that the specific 0.1- Ω thin film resistors in B have Nichrome deposited on both sides of resistors. In other cases, there is Nichrome on only one side. Therefore, B effectively has two inner resistive shells, which suggests even better flux cancellation.

B. Parasitic Inductance

The parasitic inductance of SMDCSR is measured directly with an impedance analyzer. An impedance probe is directly connected to the previous network analyzer fixtures and the impedance of the SMDCSRs can be readily obtained. Accurate measurement with the impedance analyzer requires careful calibration. The open calibration is performed by only attaching the microstrip line with nothing on it. The short calibration is performed by shorting the SMDCSR footprint with a copper foil, as shown in Fig. 14.

Only configuration A and C are shown here because of their different PCB designs. B and D should have similar parasitic inductance as A or C, respectively. The impedance measurement result is shown in Fig. 15. The inductance of a commercial coaxial shunt resistor from T&M Research is also measured here as a comparison. The inductance from the commercial coaxial shunt resistor is about 2.2 nH. The parasitic inductance of A

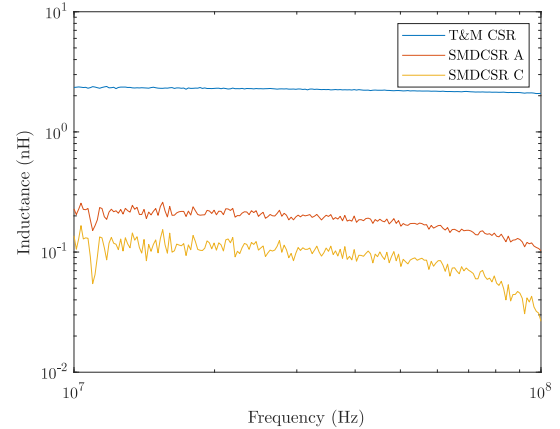


Fig. 15. SMDCSR parasitic inductance measurements.

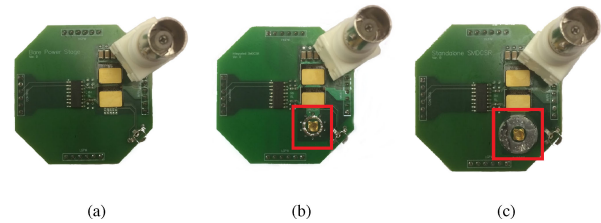


Fig. 16. Insertion inductance measurement setup. (a) Bare power stage without current measurement. (b) Integrated power stage with SMDCSR embedded (highlighted in red). (c) Power stage with standalone SMDCSR (highlighted in red).

is only about 0.22 nH, which is 1/10 that of the commercial coaxial shunt resistor. Compared to A, C has twice as many resistors in parallel and therefore has about half the parasitic inductance. The measured value is about 0.12 nH. Note that the SMDCSR inductance measurement is not as smooth as that from the commercial coaxial shunt resistor. This is because of the very low parasitic inductance and the interference from the measurement noise. Nevertheless, in addition to the high bandwidth, the SMDCSRs also demonstrate very low parasitic inductance, making them even more appealing for wide-bandgap devices dynamic characterization.

C. Total Insertion Inductance

The total insertion inductance includes not only the parasitic inductance of the SMDCSR itself but also the extra inductance due to the extra power loop area to accommodate its footprint. For a more thorough measurement of the total insertion inductance, three different double pulse test power stages are designed with GaN Systems GS66516 T GaN HFETs rated at 650 V and 60 A. The power stages are shown in Fig. 16. The bare power stage offers the baseline for the power loop inductance. Because the SMDCSR uses PCB as part of its structure, it can be easily embedded into the power stage. The integrated SMDCSR power stage is also shown in Fig. 16. Finally, another power stage with standalone SMDCSR power stage is also compared here. Because there is no current sensor in the bare power stage, its voltage measurement v_{ds} is used here as the reference waveform. Both the integrated and standalone SMDCSR uses 10 of 1.0- Ω

TABLE V
DPT MEASUREMENT SETUP

Equipment	Part No.	Bandwidth
Oscilloscope	Tektronix DPO5104B	1.0 GHz
V_{ds} Probe	Tektronix TPP0850	800 MHz
I_{ds} Sensor	SMDCSR Config. A	528 MHz

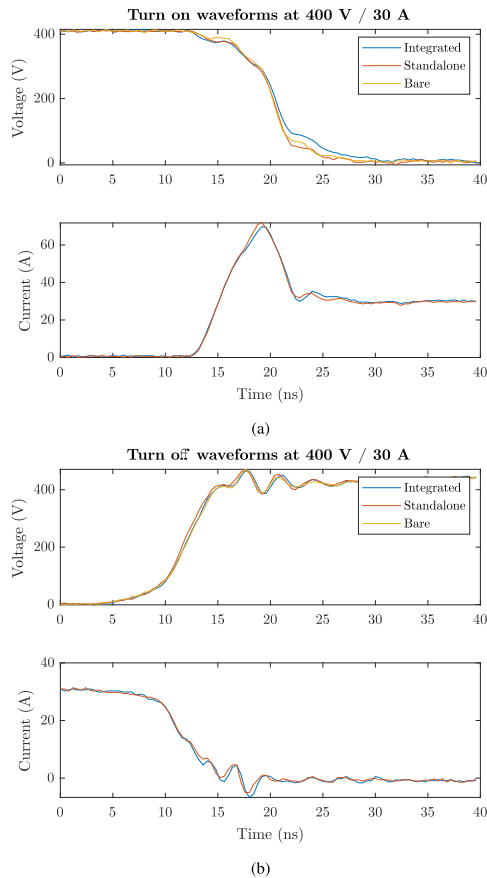


Fig. 17. Insertion inductance double pulse test waveforms comparison at with GS66516 T. (a) Turn-ON transient waveforms. (b) Turn-OFF transient waveforms.

0402 thin film resistors, or the configuration A design. The larger footprint SMDCSR configuration A is used here as a worst-case scenario for the insertion inductance. Other measurement setup details are listed in Table V. The oscilloscope sampling rate is set to 2.5 Gpts/s.

The oscilloscope captured experimental waveforms v_{ds} and i_{ds} of the device switched ON and OFF at 400 V and 30 A is shown in Fig. 17. The gate resistance here is 2.2 Ω for both turn-ON and turn-OFF. Very little difference between the three power stage can be observed. The initial voltage drop during the current rising period in the turn-ON transient is a direct indication of overall power loop inductance [4]. The small difference between the waveforms shows the insertion inductance by SMDCSR is minimal. The voltage difference during the initial voltage drop is around 7.0 V. The integrated and standalone power stage have near identical waveforms, indicating their total insertion inductance is similar. The total insertion inductance can be

TABLE VI
POWER STAGE POWER LOOP PARASITIC INDUCTANCE EXTRACTION

Power Stage	Inductance (nH)
Bare	1.89
Integrated	2.45
Standalone	2.58

estimated by

$$L_i = \frac{\Delta V}{di/dt} = 0.53 \text{ nH.} \quad (21)$$

To further verify the parasitic inductance difference because of the very small difference between the waveforms, the three power stages are analyzed in Q3D Extractor and their parasitic inductances are extracted and listed in Table VI. The difference between the bare power stage and integrated or standalone power stage is about 0.59 nH, which is very close to the 0.53 nH calculated from the measurement results. Therefore, the total insertion inductance including the extra power loop area in the worst case is less than 0.60 nH.

V. CONCLUSION

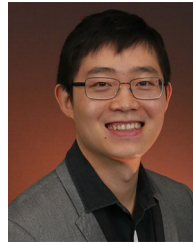
Wide-bandgap semiconductors require high bandwidth and low inductance current sensor for their dynamic characterization. The analysis on coaxial shunt resistor shows the parasitic inductance is linearly proportional to its transient thermal energy rating. The major challenge is achieving the coaxial structure in a small scale while maintaining the transient temperature rise low. The implementation of SMDCSR uses thin film resistors vertically mounted inside PCB. Placing the resistors around a circular ring mimics the coaxial structure and mitigates the flux coupling. By minimizing the gap between resistors, the SMDCSR design can achieve up to 2.23-GHz measurement bandwidth. Because small 0402 resistors are used, the parasitic inductance is quite low, and the best case shows an inductance of 0.12 nH. In the worst case, the total insertion inductance including the extra power loop area is still less than 0.60 nH. In addition to the high bandwidth and low inductance, the measurement uncertainty is kept below 0.90%, even with much more demanding heat profile than DPT. In short, SMDCSR uses the conventional commercially available cost-efficient components to meet the technical gap for wide-bandgap semiconductor dynamic characterization requirements.

The implementation of SMDCSR offers a general approach for achieving high bandwidth and low inductance resistive current sensor. Further improvements can be made on an easier assembly process to enable mass production. Even higher bandwidth or lower parasitic inductance can be achieved by paralleling a higher number of resistors or forming multiple inner resistive shells.

REFERENCES

- [1] J. Millan, P. Godignon, X. Perpina, A. Perez-Tomas, and J. Rebollo, "A survey of wide bandgap power semiconductor devices," *IEEE Trans. Power Electron.*, vol. 29, no. 5, pp. 2155–2163, May 2014.

- [2] Z. Zhang *et al.*, "Methodology for switching characterization evaluation of wide band-gap devices in a phase-leg configuration," in *Proc. 29th Annu. Appl. Power Electron. Conf. Expo.*, 2014, pp. 2534–2541.
- [3] M. Danilovic, Z. Chen, R. Wang, F. Luo, D. Boroyevich, and P. Mattavelli, "Evaluation of the switching characteristics of a gallium-nitride transistor," in *Proc. IEEE Energy Convers. Congr. Expo.: Energy Convers. Innov. Clean Energy Future*, 2011, pp. 2681–2688.
- [4] E. A. Jones *et al.*, "Characterization of an enhancement-mode 650-V GaN HFET," in *Proc. IEEE Energy Convers. Congr. Expo.*, 2015, pp. 400–407.
- [5] "Current Viewing Resistors," T&M Research, Albuquerque, NM, USA, 2020. [Online]. Available: <http://www.tandmresearch.com/>
- [6] W. Zhang, Z. Zhang, and F. Wang, "Review and bandwidth measurement of coaxial shunt resistors for surge-current measurements," in *Proc. IEEE Energy Convers. Congr. Expo.*, 2019, pp. 3259–3264.
- [7] "Precision Thin Film Technology," Vishay, Malvern, PA, USA, 2020. [Online]. Available: www.vishay.com
- [8] J. A. Ferreira, W. A. Cronje, and W. A. Relihan, "Integration of high frequency current shunts in power electronic circuits," *IEEE Annu. Power Electron. Specialists Conf.*, vol. 10, no. 1, pp. 1284–1290, 1992.
- [9] J. H. Park, "Shunts and inductors for surge-current measurements," *J. Res. Nat. Bureau Standards*, vol. 39, no. 3, pp. 191–212, 1947.
- [10] J. C. Hernandez, L. P. Petersen, M. A. E. Andersen, and N. H. Petersen, "Ultrafast switching superjunction MOSFETs for single phase PFC applications," in *Proc. 29th Annu. Appl. Power Electron. Conf. Expo.*, 2014, pp. 143–149.
- [11] A. J. L. Joannou, D. C. Pentz, J. D. van Wyk, and A. S. de Beer, "Some considerations for miniaturized measurement shunts in high frequency power electronic converters," in *Proc. 16th Eur. Conf. Power Electron. Appl.*, 2014, pp. 1–7.
- [12] "CWT MiniHF," Power Electronics Measurement, Nottingham, U.K., 2020. [Online]. Available: <http://pemuk.com>
- [13] J. Wang *et al.*, "Infinity Sensor: Temperature Sensing in GaN Power Devices using Peak di/dt," in *Proc. IEEE Energy Convers. Congr. Expo.*, 2018, pp. 884–890.
- [14] "Pearson Current Monitor," Pearson Electronics, Palo Alto, CA, USA, 2020. [Online]. Available: <https://www.pearsonelectronics.com/pdf/7713-03.pdf>
- [15] MANGANIN. Isabellenhütte, 2020. [Online]. Available: <https://www.isabellenhuette.de/en/precision-alloys/products/manganin/>
- [16] Z. Zhang, B. Guo, F. F. Wang, E. A. Jones, L. M. Tolbert, and B. J. Blalock, "Methodology for wide band-gap device dynamic characterization," *IEEE Trans. Power Electron.*, vol. 32, no. 12, pp. 9307–9318, Dec. 2017.
- [17] Z. Chen, "Characterization and modeling of high-switching-speed behavior of SiC active devices," M.S. Thesis, Virginia Tech, Blacksburg, VA, USA, 2009.
- [18] "Thin Film Resistors," SUSUMU, Kyoto, Japan, 2020. [Online]. Available: <https://www.susumu.co.jp/english/product/category.php?cid=8>
- [19] W. S. Levine, *The Control Handbook*. Boca Raton, FL, USA: CRC press, 2010.
- [20] "Network Analyzers," Keysight Technologies, Santa Rosa, CA, USA. [Online]. Available: <https://www.keysight.com/en/pcx-x2015001/networkanalyzers>



Zheyu Zhang (Senior Member, IEEE) received the B.S. and M.S. degrees from Huazhong University of Science and Technology, Wuhan, China, in 2008 and 2011, respectively, and the Ph.D. degree from The University of Tennessee, Knoxville, TN, USA, in 2015, all in electrical engineering.

He is the Warren H. Owen Duke Energy Assistant Professor of engineering with Clemson University, Clemson, SC, USA. He was a Research Assistant Professor with the Department of Electrical Engineering and Computer Science at the University of Tennessee, from 2015 to 2018. He joined General Electric Research, as the Lead Power Electronics Engineer at Niskayuna, NY, USA from 2018 to 2019. He has authored or coauthored over 90 papers in the most prestigious journals and conference proceedings, filed over ten patent applications with one licensed, authored one book, and presented four IEEE tutorial seminars. His research interests include wide band-gap based power electronics, modularity and scalability technology, medium voltage power electronics, and highly efficient, ultra-dense, cost-effective power conversion systems for electric propulsion, electrified transportation, renewables, energy storage, and grid applications.

Dr. Zhang was the recipient of two Prize Paper Awards from the IEEE Industry Applications Society and IEEE Power Electronics Society. He is currently an Associate Editor for IEEE TRANSACTIONS ON POWER ELECTRONICS and IEEE TRANSACTIONS ON INDUSTRY APPLICATIONS. He is a senior member of IEEE.



Fei Wang (Fellow, IEEE) received the B.S. degree from Xian Jiaotong University, Xian, China, in 1982, and the M.S. and Ph.D. degrees from the University of Southern California, Los Angeles, CA, USA, in 1985 and 1990, respectively, all in electrical engineering.

He was a Research Scientist with the Electric Power Lab, University of Southern California, from 1990 to 1992. He joined the GE Power Systems Engineering Department, Schenectady, NY, USA, as an Application Engineer in 1992. From 1994 to 2000, he was a Senior Product Development Engineer with GE Industrial Systems, Salem, VA, USA. During 2000 to 2001, he was the Manager with the Electronic and Photonic Systems Technology Lab, GE Global Research Center, Schenectady, NY, USA, and Shanghai, China. In 2001, he joined as a Research Associate Professor with the Center for Power Electronics Systems (CPES) at Virginia Tech, Blacksburg, VA, USA, where he became an Associate Professor in 2004. From 2003 to 2009, he also served as the CPES Technical Director. Since 2009, he has been with The University of Tennessee and Oak Ridge National Lab, Knoxville, TN, USA, as a Professor and the Condra Chair of Excellence in Power Electronics. He is a Founding Member and the Technical Director of the multiuniversity NSF/DOE Engineering Research Center for Ultrawide-area Resilient Electric Energy Transmission Networks (CURENT) led by The University of Tennessee. His research interests include power electronics and power systems.

Dr. Wang is a fellow of the U.S. National Academy of Inventors.



Edward V. Brush received the B.S. and M.S. degrees from the University of Virginia, Charlottesville, VA, USA, in 2001 and 2006, respectively.

He is currently an RF R&D Hardware Engineer for the Oscilloscope Product Division at Keysight Technologies, Santa Rosa, CA, USA. He also worked with Agilent Technologies in Colorado Springs, CO, USA. He has been involved in the design of oscilloscope probes including differential voltage probes, current probes, and voltage rail probes.



Wen Zhang (Student Member, IEEE) received the B.S. degree in electrical engineering from the Huazhong University of Science and Technology, Wuhan, China, in 2015, and the M.S. degree in electrical engineering in 2019 from the University of Tennessee, Knoxville, TN, USA, where he is currently working toward the Ph.D. degree with the University of Tennessee.

His research interests include wide-bandgap semiconductors and their applications, motor drives and filters, and sensing technologies.



Neil Forcier received the bachelor's degree in electrical engineering from The Pennsylvania State University, University Park Campus, PA, USA, in 2007.

He served in the US Navy for six years as an Electronic Technician, performing repair and calibration of electronic test and measurement equipment. He has been worked with Agilent / Keysight Technologies for the last 14 years in a variety of different roles including Application Engineer, R&D Engineer, and Strategic Planner.